Palaeogeography, Palaeoclimatology, Palaeoecology 623 (2023) 111634

Contents lists available at ScienceDirect

Palaeogeography, Palaeoclimatology, Palaeoecology

journal homepage: www.elsevier.com/locate/palaeo

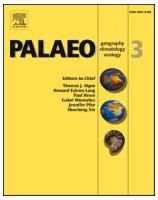

Volcanism intensity and associated climate-ocean-land dynamics during the Cryogenian interglaciation: Insights from mercury isotopes

Li Wang [a,b], Yu Liu [a], Chenchen Yang [a,b], Hu Huang [a], Mingcai Hou [a], Chuang Yang [b,c], Runsheng Yin [b,*]

[a] Institute of Sedimentary Geology, Chengdu University of Technology, Chengdu 610059, China
[b] State Key Laboratory of Ore Deposit Geochemistry, Institute of Geochemistry, Chinese Academy of Sciences, Guiyang 550081, China
[c] University of Chinese Academy of Sciences, Beijing 100049, China

ARTICLE INFO

Editor: A Dickson

Keywords:
Volcanism
Climate-ocean-land dynamics
Cryogenian interglaciation
Mercury
Isotope

ABSTRACT

The Cryogenian interglaciation (ca. 660 Ma to 650 Ma) was an interlude between the Sturtian glaciation (ca. 717 Ma to 660 Ma) and Marinoan glaciation (ca. 650 Ma to 635 Ma). Recent observations of anomalously high mercury (Hg) concentrations in Cryogenian interglacial sediments at basinal settings in the Nanhua Rift Basin, South China, imply that large volcanism can be a possible driving force of the Cryogenian interglaciation. To test this hypothesis and understand the potential linkage between large volcanism and climate-ocean-land dynamics during the Cryogenian interglaciation, we investigate mercury (Hg) concentrations and isotopic composition of Cryogenian interglacial sediments at shallow water (shelf/slope) settings in the Nanhua Rift Basin, South China. The basal Mn-bearing black shales show an increased pattern in Hg concentrations (318 to 4400 ppb) and Hg/TOC ratios (243 to 1730 ppb/wt%), and overall positive Δ^{199}Hg values (0.00 to 0.10‰), suggesting increasing volcanic Hg input into the ocean via atmospheric Hg(II) deposition in the early Cryogenian interglaciation. The upper siltstone samples show a dramatic decrease in Hg concentrations (from 5110 to 459 ppb) and a drop of Δ^{199}Hg values (from 0.04 to −0.05‰), suggesting weakened volcanism during the middle-late Cryogenian interglaciation. Combined with the analyses of major and trace elements proxies, we demonstrate that (1) greenhouse climate in the early Cryogenian interglaciation induced high oceanic productivity, high organic burial on the seafloor and high terrestrial sulfate input into the ocean, which favors the deposition of Mn-bearing black shales in the ocean; and (2) weakened volcanism and continued continental weathering exhausted atmospheric CO_2 and drove the global climate to the Marinoan glaciation. This study, therefore, provides important insights into the climate-ocean-land dynamics during the Cryogenian interglaciation.

1. Introduction

During the Cryogenian (ca. 717 Ma to 635 Ma) in the middle Neoproterozoic, the breakup of the Rodinia supercontinent was accompanied by two global glaciation events named the Sturtian glaciation (ca. 717 Ma to 660 Ma) and the Marinoan glaciation (ca. 650 Ma to 635 Ma), punctuated by a brief nonglacial interlude named the Cryogenian interglaciation (ca. 660 Ma to 650 Ma) (Hoffman et al., 1998; Li et al., 2008; Rooney et al., 2015; Hoffman et al., 2017). Large volcanism, which emits large amounts of greenhouse gases (e.g., CO_2) into the environment, is believed as a possible driving force for the Cryogenian interglaciation (Hoffman et al., 1998, 2017). Zhou et al. (2019), based on high-precision U—Pb zircon chemical abrasion-isotope dilution–thermal ionization mass spectrometry, yielded an age of 658.80 ± 0.50 Ma, providing a new age constraint for the termination of the Sturtian glaciation. Li et al. (2012), based on Fe, C, Mo, and S chemostratigraphic data of the Cryogenian Datangpo Formation, proposed a stratified redox model for fluctuations in water chemistry and depositional environment during the Cryogenian interglaciation. The linkage between large volcanism and environmental changes during the Cryogenian interglaciation is yet poorly understood, however.

The global ocean of the Cryogenian interglaciation was associated with a worldwide deposition of metalliferous black shales containing manganese (Mn) resources of great economic importance (Xu et al., 2019; Tan et al., 2021). These black shales record profound changes in oceanic redox and productivity during the Cryogenian interglaciation.

* Corresponding author at: State Key Laboratory of Ore Deposit Geochemistry, Institute of Geochemistry, Chinese Academy of Sciences, Guiyang 550081, China.
E-mail address: yinrunsheng@mail.gyig.ac.cn (R. Yin).

https://doi.org/10.1016/j.palaeo.2023.111634
Received 3 October 2022; Received in revised form 3 May 2023; Accepted 8 May 2023
Available online 11 May 2023

Large volcanism, such as large igneous provinces (LIPs) eruptions, can result in transit emission of large amounts of mercury (Hg) to the environment. This Hg could transport globally in the atmosphere and subsequently deposits into land and ocean systems, resulting in anomalous high Hg concentrations in global soil and marine sediments (Grasby et al., 2019). Mercury is hosted in sediments in multiple phases, including organic matter, sulfides, and clay minerals (Them et al., 2019; Shen et al., 2020). Recent studies suggest that anomalously high Hg to total organic carbon (Hg/TOC) ratios can be a useful proxy for tracing large volcanism in geological history (Grasby et al., 2019; Shen et al., 2020), although studies also suggest that the depositional environments may play a critical role in Hg accumulation in sediments rather than input sources (Shen et al., 2022; Xue et al., 2022). Besides, caution must be paid to weathered rocks because Hg may be lost during silicate weathering (Charbonnier et al., 2020; Park et al., 2022). A recent study observed anomalously high Hg/TOC ratios in Cryogenian black shales from a basinal setting in the Nanhua Rift Basin, South China, which provide possible support for large volcanism in triggering the Cryogenian interglaciation (Zhou et al., 2021).

Mercury isotopes (^{196}Hg, ^{198}Hg, ^{199}Hg, ^{200}Hg, ^{201}Hg, ^{202}Hg, and ^{204}Hg) can aid in understanding the sources and processes of Hg in the environment, as they can undergo both mass-dependent fractionation (MDF, reported as δ^{202}Hg) and mass-independent fractionation (MIF, reported as Δ^{199}Hg). Unlike that Hg-MDF occurs during a variety of physical, chemical, and biological processes, Hg-MIF mainly occurs during photochemical reactions with limited influence from other processes (Bergquist and Blum, 2007; Blum et al., 2014). Sedimentation, diagenesis, and metamorphism processes do not trigger Hg-MIF, allowing the use of Δ^{199}Hg in sedimentary records for understanding Hg geochemical cycles in geological history (Grasby et al., 2019; Chen et al., 2022; Liu et al., 2022). Although volcanic Hg emitted from various tectonic systems have variable Δ^{199}Hg values (Zambardi et al., 2009; Moynier et al., 2021; Yin et al., 2022), the MIF signature of volcanic Hg can be modulated by Hg(II) photoreduction process on Earth's surface, leading to negative Δ^{199}Hg values of gaseous Hg(0) and positive Δ^{199}Hg values of aqueous Hg(II) species (Bergquist and Blum, 2007; Blum et al., 2014).

Zhou et al. (2021) reported high Hg/TOC ratios and positive Δ^{199}Hg excursions in Cryogenian black shales from a basinal setting in the Nanhua Rift Basin, South China, highlighting enhanced volcanic Hg input to open oceans via wet Hg(II) deposition. However, Hg records at shallow water (shelf/slope) settings have yet not been investigated, limiting our understanding of the strength of volcanisms in causing the Cryogenian interglaciation. To fill this knowledge gap, here we investigate Hg concentrations and isotopic composition of Cryogenian interglacial deposits at shallow water (shelf/slope) settings of the Nanhua Rift Basin, South China. In combination with multiple geochemical proxies (major and trace elements, total sulfur (TS), and TOC concentrations), this study attempts to evaluate the influence of large volcanism on the shallow water environment and understand the climate-ocean-land dynamics, during the Cryogenian interglaciation.

2. Geological background

The Nahua Rift Basin in South China (Fig. 1) was formed at ca. 820 Ma after the breakup of the Rodinia supercontinent (Wang and Li, 2003). The increased thickness of Cryogenian sediments from northwest to southeast of the Nanhua Rift Basin indicates an increase in seawater depth along the NW-SE axis of the basin during the Cryogenian (Wang and Li, 2003; Li et al., 2012). The Cryogenian sediments consist of the Tiesi'ao Formation (Sturtian glaciation equivalent), the Datangpo Formation (Cryogenian interglaciation equivalent) and the Nantuo Formation (Marinoan glaciation equivalent) (Zhang et al., 2003). The glacial Tiesi'ao and Nantuo formations consist mainly of massive or stratified diamictite (Yu et al., 2016; Zhou et al., 2021). The interglacial Datangpo Formation can be divided into two members: the lower Member I consists mainly of Mn-bearing black shales (Mn-carbonate exists at the bottom), and the upper Member II consists mainly of black shales and siltstones (Yu et al., 2016; Zhu et al., 2019; Zhou et al., 2021).

The studied drill core (ZK0202) was collected from Xiushan, at shelf/

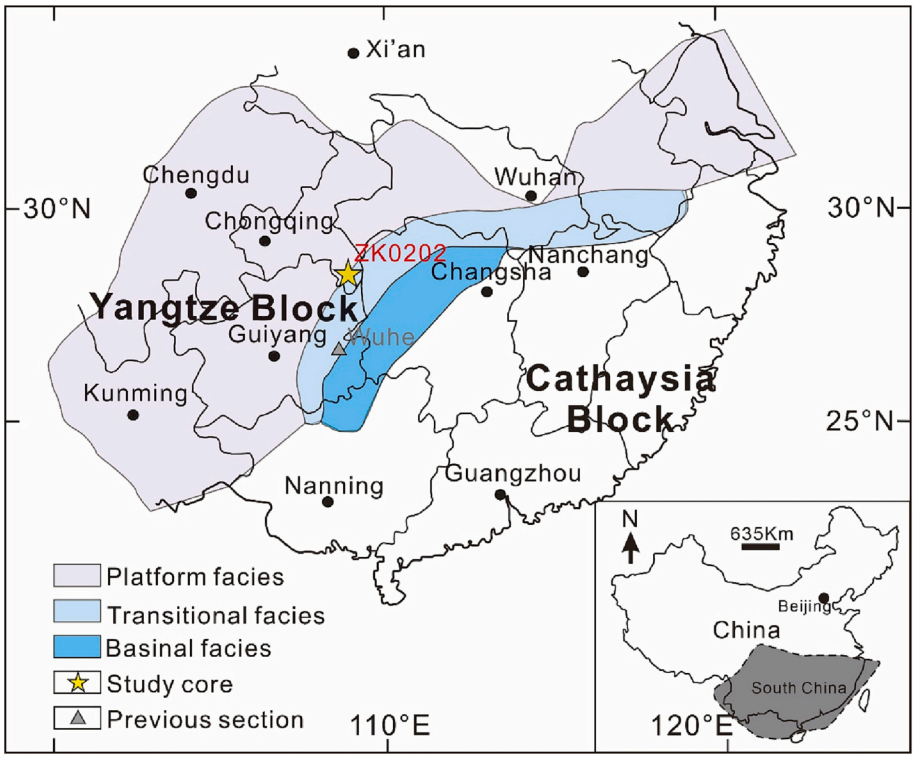

Fig. 1. Simplified paleogeographic map showing South China in the Cryogenian interglacial interval and location of drillcore ZK0202 and the Wuhe Section (modified from Zhou et al., 2019; Zhou et al., 2021).

slope settings of the Nanhua Rift Basin, and the previously studied Wuhe section was at transition/basinal settings of the Nanhua Basin (Fig. 1; Zhou et al., 2021). From bottom to top (Fig. 2), the Datangpo Formation in ZK0202 core can be divided into (1) Member I: Mn-bearing black shale (~ 24 m thick); (2) Member II_1: dark grey-black argillaceous siltstone interbedded with grey-black shale (~ 8 m thick); and (3) Member II_2: grey-dark grey siltstone (~ 7 m thick). The thickness of the Datangpo Formation in ZK0202 is much higher than that observed in the Wuhe Section, i.e., Member $I = 0.3$ m, and Member II = 8 m (Zhou et al., 2021).

3. Methods

A total of 45 samples were collected from the Datangpo Formation in core ZK0202. Details of the samples (lithology and depth) were shown in Fig. 2 and Supplementary **Table S1**. All samples were cleaned, air-dried, powdered to 150 mesh and homogenized, prior to chemical analysis at the Institute of Geochemistry, Chinese Academy of Sciences.

3.1. Major and trace element analyses

The powdered samples were fused with lithium metaborate or lithium borate at 1100 °C, cooled to produce a glass disk, and then analyzed by ARL Perform' X 4200 X-ray fluorescence spectrometry, with an analytical uncertainty of less than ±5%. The detailed analytical procedures were described by (Franzini et al., 1972). The Chemical index of alteration (CIA), indicative of the degree of chemical weathering, was calculated based on the following equation (Nesbitt and Young, 1982):

$$CIA = Al_2O_3/(Al_2O_3 + CaO^* + Na_2O + K_2O) \times 100 \quad (1)$$

where all oxides are calculated in molar proportions. CaO* only corresponds to CaO from silicates. For this study, CaO was corrected for phosphate using P_2O_5 data ($CaO^* = CaO - 10/3 \times P_2O_5$). If $CaO^*/Na_2O < 1$, the CaO* values were used. Otherwise, CaO* is replaced by Na_2O.

Whole-rock trace elements were analyzed with Plasma Quant-MS Elite inductively coupled plasma–mass spectrometer (Qi et al., 2000). Both procedural blanks and the national standards OU-6, AMH-1, and GBPG-1 were analyzed for data quality control, which yielded an average recovery of 90% ($n = 3$) and reproducibility within less than ±10% for all trace elements.

3.2. Total sulfur and total organic carbon

Total sulfur (TS) and total organic carbon (TOC) concentrations were analyzed using an Elementar Vario Microcube analyzer with analytical errors of less than ±2.5%. For TOC analysis, the sample powders were leached with hydrochloric acid to remove inorganic carbon. The residual powder was then rinsed with 18.2 MΩ·cm water and freeze-dried.

3.3. Mercury content and isotope analyses

Total mercury (THg) concentrations were analyzed using a Lumex R915 + Hg analyzer (limit of detection: 0.5 ng/g Hg), which yielded THg recoveries of 90 to 110% for the standard reference material (GSS-5, soil, $n = 4$) and a relative standard deviation of <10% for sample duplicates.

Zhou et al. (2021) employed a dual-stage combustion furnace to preconcentrate Hg from low Hg samples into 5 mL of 40% reverse aqua regia ($HCl/HNO_3 = 1/3$, V/V). In this study, the acid digestion method was adopted to prepare the samples investigated, due to their high Hg concentrations. Briefly, about 0.2 g of samples were digested in 2 mL aqua regia ($HCl/HNO_3 = 3/1$, V/V) at 95 °C for 3 h. The acid digestion method yielded Hg recoveries of 90 to 110% for the samples, compared to Hg concentrations measured by the Lumex R915+ Hg analyzer. The digested sample solutions were diluted to 0.5 ng/g Hg in 10–20% acid matrices and then measured by a Neptune Plus multi-collector inductively coupled plasma–mass spectrometer (Yin et al., 2016). Following the nomenclature recommended by Bergquist and Blum (2007), Hg-MDF is expressed in $\delta^{202}Hg$ notation in units of per mil (‰) referenced to the NIST-3133 Hg standard:

$$\delta^{202}Hg\ (‰) = \left[\left(^{202}Hg/^{198}Hg_{sample}\right)/\left(^{202}Hg/^{198}Hg_{standard}\right) - 1\right] \times 1000 \quad (2)$$

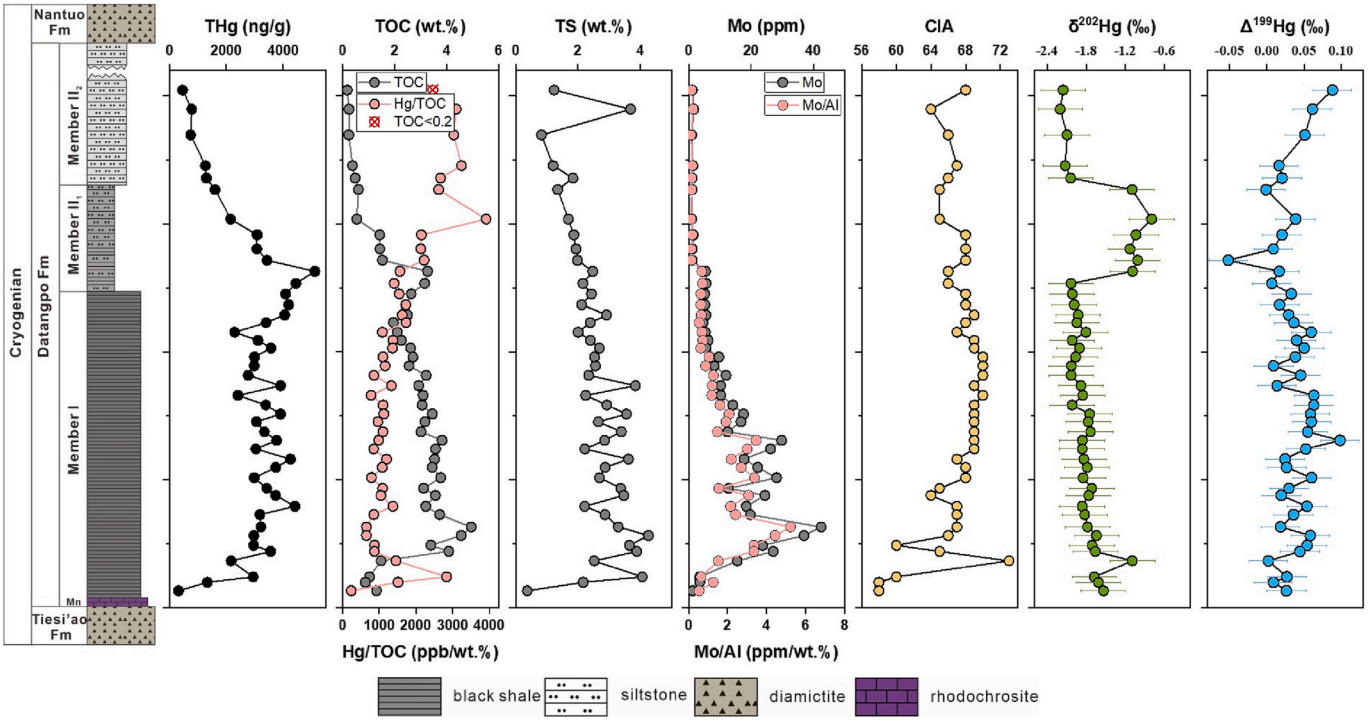

Fig. 2. Profiles of Hg, TOC, TS, CIA, Mo, Hg isotopes, Hg/TOC and Mo/Al ratios in the Cryogenian interglacial interval in the drillcore ZK0202, South China.

Mass independent fractionation of Hg isotopes is reported in Δ notation:

$$\Delta^{xxx}Hg\ (‰) \approx \delta^{xxx}Hg - \delta^{202}Hg \times \beta \quad (3)$$

$\beta = 0.2520$ for ^{199}Hg, 0.5024 for ^{200}Hg, and 0.7520 for ^{201}Hg (Blum and Bergquist, 2007). NIST-3177 secondary standard solutions, diluted to 0.5 ng/mL Hg in 10% acid, were measured in every 10 samples, which yielded $\delta^{202}Hg$ of −0.58 ± 0.10‰, $\Delta^{199}Hg$ of −0.01 ± 0.09‰ and $\Delta^{201}Hg$ of −0.06 ± 0.11‰ (2SD, n = 15). Measurement of GSS-4 digested solutions yielded $\delta^{202}Hg$ of −1.67 ± 0.27‰, $\Delta^{199}Hg$ of −0.46 ± 0.10‰, $\Delta^{200}Hg$: −0.03 ± 0.09‰; and $\Delta^{201}Hg$ of −0.41 ± 0.08‰ (2SD, n = 10). The largest 2SD values for NIST-3177 and GSS-4 reflect the analytical uncertainties of our samples.

4. Results

The analytical results are summarized in **Table S1** and illustrated in Fig. 2. Mn-bearing black shales in Member I show overall high THg concentrations (318 to 4400 ppb), negative $\delta^{202}Hg$ values (−2.03 to −1.09‰), and near-zero to slightly positive $\Delta^{199}Hg$ values (0.00 to 0.10‰). The values of TOC and TS (2 to 5 wt% for both), Hg/TOC (243 to 1730 ppb/wt%) and CIA (58 to 73) abruptly increase at the base of Member I. Anomalously high peaks of Mo concentration (1.31 to 42.50 ppm) and Mo/Al ratio (0.54 to 5.23 ppm/wt%) are observed in Member I.

Siltstones and grey-black shales in Member II_1 first show the highest THg (up to 5110 ppb), TOC (up to 3.27 wt%), and TS (up to 2.47 wt%) concentrations, and then show a rapid decrease of THg (down to 1600 ppb), TOC (down to 0.55 wt%) and TS (down to 1.35 wt%) concentrations. Hg/TOC ratios show a general increasing pattern in the entire Member II_1 (1410 to 3910 ppb/wt%). $\Delta^{199}Hg$ values are near-zero (−0.05 to 0.04‰). An abrupt positive excursion of $\delta^{202}Hg$ to about −1‰ can be observed. The Member II_1 samples show medium CIA values (65 to 68), and low Mo concentrations (1.01 to 5.62 ppm) and Mo/Al ratios (0.71 to 0.13 ppm/wt%).

Siltstones in Member II_2 show the lowest THg (459 to 1300 ppb), TOC (0.19 to 0.49 wt%) and TS (0.83 to 3.69 wt%) concentrations. In Member II_2, Hg/TOC ratios are the highest (2460 to 3240 ppb/wt%), $\Delta^{199}Hg$ shifts to slightly positive values (0.02 to 0.09‰), and $\delta^{202}Hg$ shifts to more negative values (−2.20 to −2.04 ‰). The Member II_2 samples also show medium CIA values (64 to 68), and the lowest Mo concentrations (1.02 to 1.70 ppm) and Mo/Al ratios (0.13 to 0.23 ppm/wt%).

5. Discussion

5.1. Mercury host phases in Cryogenian interglacial sediments

Possible host phases of Hg in sediments include organic matter, sulfides, and clay minerals (Krupp, 1988; Grasby et al., 2019; Shen et al., 2019, 2020). Mercury has a strong affinity to the organic matter in normal sediments (Grasby et al., 2019; Shen et al., 2020), however recent studies have suggested that sulfides (e.g., pyrite) can be another important host of Hg in sulfidic water conditions (Shen et al., 2019, 2022). Besides, Hg in sediments can also be adsorbed onto the surface of clay minerals due to their high specific surface areas (Krupp, 1988). As shown in Fig. 3, slightly positive correlations between THg and TOC (r = 0.48), TS (r = 0.53), and Al (r = 0.61) in Member I samples, suggesting Hg is hosted in multiple phases (organic matter, sulfides, and clay minerals). Member I samples show the highest TOC and TS concentrations, implying elevated oceanic productivity in the surface ocean and sulfidic conditions in deep water columns during this period (see

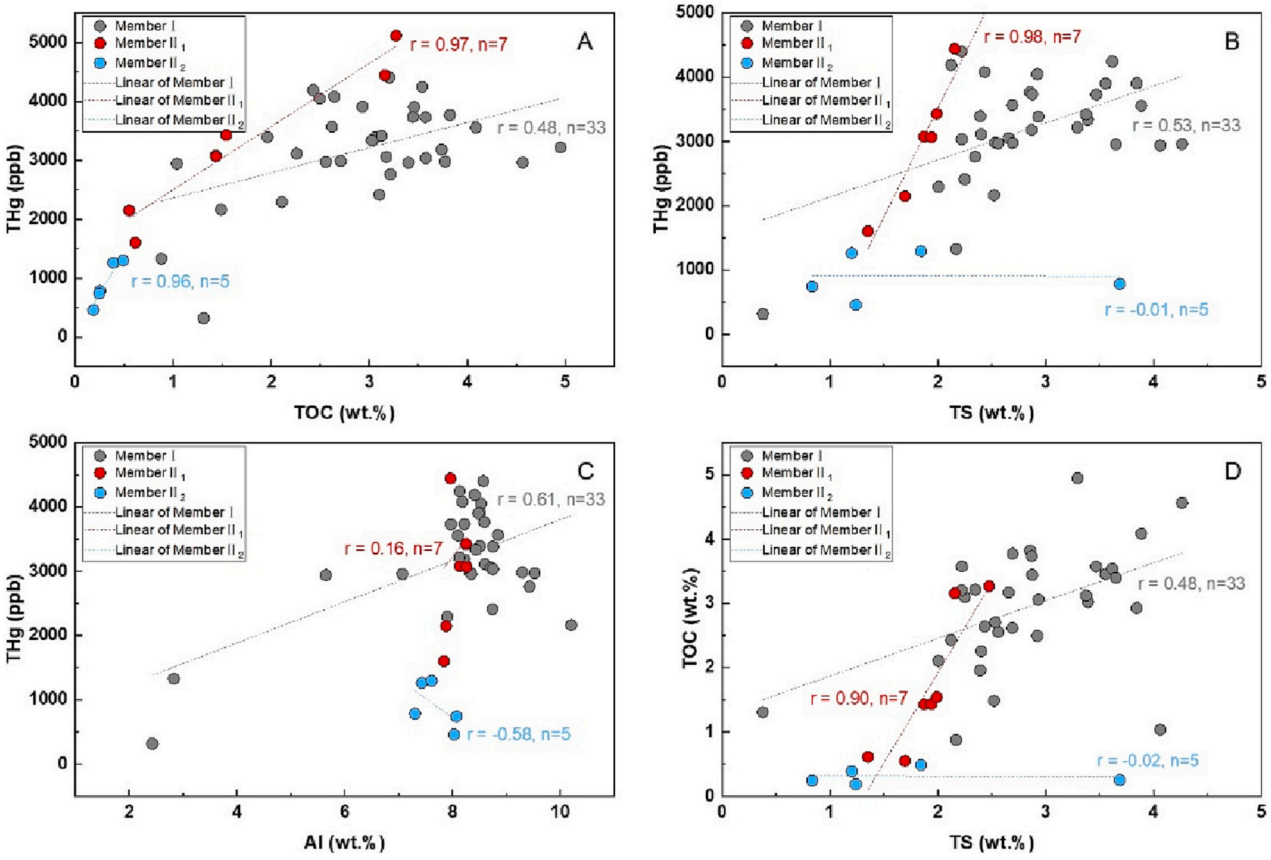

Fig. 3. Correlations between (A) TOC and Hg; (B) TS and Hg; (C) TOC and TS; and (D) Al and Hg in the Cryogenian interglacial interval in drillcore ZK0202, South China.

discussion in Section 5.3). Both organic matter and sulfides are believed to scavenge a large amount of Hg(II) deposited into the ocean, due to their high affinity to Hg (see discussion in Section 5.2.1). This is supported by the near-zero to slightly positive Δ^{199}Hg values for Member I samples (0.00 to 0.10‰), given that atmospheric Hg(II) has positive Δ^{199}Hg values (Bergquist and Blum, 2007; Blum et al., 2014). In addition, the positive correlation between THg and Al in Member I samples may suggest that a substantial amount of Hg was also scavenged by clay minerals imported into the ocean. The high CIA values in Member I samples suggest enhanced continental weathering and enhanced input of terrestrial clay minerals into the ocean. The Member II_1 samples show strongly positive correlations between THg and TOC ($r = 0.97$), and TS ($r = 0.98$), but a poor correlation between THg and Al ($r = 0.16$), suggesting that Hg is hosted in the organic matter and sulfides. The THg-TS relationship may be a by-product of TOC-TS covariation ($r = 0.90$) due to organic matter containing many sulfur-containing groups (e.g., thiol (-SH) groups). The Member II_2 samples show a strong correlation between THg and TOC ($r = 0.96$) but weak correlations between THg and TS ($r = -0.01$), and Al ($r = -0.58$), suggesting Hg of sediment is also mainly hosted in organic matter. Notably, positive correlations between Hg and TOC have been widely observed in ancient and modern ocean sediments (Grasby et al., 2019; Shen et al., 2019, 2020; Xue et al., 2019). Here, we infer that Hg in Member II_1 and II_2 samples is mainly hosted in organic matter, different from the multiple hosts of Hg in Member I samples.

5.2. Variation of volcanic intensity in the Cryogenian interglaciation

5.2.1. Large-scale volcanism in the early Cryogenian interglaciation

Changes in Hg concentrations and Hg/TOC ratios in sediments can roughly represent the intensity of volcanic Hg input (Grasby et al., 2019; Shen et al., 2019, 2020). In this study, THg contents and Hg/TOC ratios of the Member I samples (318 to 4400 ppb and 243 to 1730 ppb/wt%, respectively) are much higher than that observed in average marine sediments (62.4 ppb and 71.9 ppb/wt%, respectively; Grasby et al., 2019) and the recently reported elevated Hg concentrations and Hg/TOC ratios (76 to 366 ppb and 114 to 717 ppb/wt%, respectively; Zhou et al., 2021) in the equivalent black shales in the basinal Wuhe section, Nanhua Basin. This confirms the previous hypothesis on the presence of large-scale volcanism at the onset of the Cryogenian interglaciation (Zhou et al., 2021), and implies that shallow water (shelf/slope) settings received more volcanic Hg than basinal settings, possibly due to the closer location of shallow-water environments to volcanic emissions. Large-scale volcanism during the Cryogenian interglaciation is possibly related to enhanced global continental arc activity during the middle-late Cryogenian (McKenzie et al., 2016; Cao et al., 2017), or LIP and rifting activities due to the breakup of the Rodina supercontinent (mainly from ca. 900 Ma ~ 700 Ma; Ernst et al., 2008; Li et al., 2008). A recent study discovered abundant mafic-ultra mafic dike swarms of ca. 700– 650 Ma along the northern margin of the Yangtze Block, which could be a result of a LIP event (Zhao et al., 2018). Volcanic activities mentioned above could have released large amounts of CO_2, triggering the Cryogenian interglaciation (Zhou et al., 2021). Besides, the heating of organic-rich sediments from sill intrusion during volcanisms could also result in the release of Hg and CO_2 into the atmosphere (Liu et al., 2022).

Mercury isotopic composition of these samples can provide insights into the pathways of volcanic Hg entering the ocean. The negative δ^{202}Hg values (δ^{202}Hg: −1.81‰ ± 0.18‰) of the samples fall into the range of that reported for global marine sediments (Blum et al., 2014). However, either change in Hg sources or biogeochemical processes is required to explain changes in δ^{202}Hg (Blum et al., 2014). In contrast, Hg-MIF is primarily caused via photochemical reactions with limited influence from other processes, enabling the use of Δ^{199}Hg for tracing pathways of Hg entering the ocean. The Δ^{199}Hg value of volcanic Hg (~ 0‰, Zambardi et al., 2009) can be modulated by aqueous Hg(II) photoreduction (Bergquist and Blum, 2007). Hg(II) photoreduction in cloud droplets results in negative Δ^{199}Hg values in the gaseous Hg(0) species and leaves positive Δ^{199}Hg values in residual gaseous Hg(II) pool (Blum et al., 2014). The terrestrial system preferentially accumulates Hg (0) and is normally characterized by negative Δ^{199}Hg values (Yin et al., 2013; Blum et al., 2014). However, Hg(II) is water-soluble and readily enters the ocean via wet deposition (precipitation). The positive Δ^{199}Hg values (0.00 to 0.10‰) of Member I samples suggest strong input of volcanic Hg via wet Hg(II) deposition during the early Cryogenian interglaciation.

5.2.2. Weakened volcanism in the middle-late Cryogenian interglaciation

The lower Hg concentrations and the characteristics of Hg isotopes in Member II samples (Fig. 2) may suggest weakened volcanism during the middle-late Cryogenian interglaciation. Although Member II samples show an increase in Hg/TOC ratios, this is likely due to the dramatic decrease in TOC content in these samples (Fig. 2).

The ocean receives Hg via atmospheric Hg(II) deposition and terrestrial runoff (Yin et al., 2015). The Member II_1 samples show a sharp decrease in THg concentrations and δ^{202}Hg (to −1‰), which would suggest a sudden weakening of volcanic Hg input to the ocean via wet Hg(II) deposition, associated with continuous enhance input of terrestrial Hg (Grasby et al., 2017; Them et al., 2019). Terrestrial Hg in South China during the Precambrian was believed to have higher δ^{202}Hg of ~ −1‰ (Fan et al., 2021). If volcanic Hg input into the ocean was significantly decreased, the Hg isotopic signature of Member II_1 samples would be dominant by that of the enhanced terrestrial Hg sources. Indeed, the negative Δ^{199}Hg excursions in the lower Member II_1 samples support this hypothesis, given terrestrial Hg has negative Δ^{199}Hg values (Yin et al., 2013; Blum et al., 2014). In contrast, the Member II_2 samples (δ^{202}Hg: −2.12‰ ± 0.06‰; Δ^{199}Hg: 0.05‰ ± 0.03‰) show similar Hg isotopic characteristics with ancient and modern marine sediments deposited under normal conditions (Grasby et al., 2019; Shen et al., 2019, 2020; Yin et al., 2015, 2017), which have received Hg mainly through atmospheric Hg(II) deposition, with limited input from terrestrial sources. By analogy, the lowest Hg concentrations with positive Δ^{199}Hg values of Member II_2 samples would suggest a dominant input of Hg to the ocean via normal Hg(II) deposition, in the absence of large volcanism. Terrestrial Hg input would have played a less important role in contributing Hg into the ocean, as supported by the slight decrease of CIA in Member II_2 samples.

5.3. Climate-ocean-land dynamics during the Cryogenian interglaciation

In this study, Hg and other paleoclimatic proxies (e.g., major and trace elements, TS and TOC concentrations) provide an integrated insight into the climate-ocean-land dynamics during the Cryogenian interglaciation, which can be divided into three stages as follows.

Stage I (Fig. 4A): Large-scale volcanism in the early Cryogenian interglaciation, as revealed by high Hg concentrations and Hg/TOC ratios in Member I Mn-bearing black shales, would emit large volumes of CO_2 to the atmosphere, triggering global warming and termination of the Sturtian glaciation. Volcanic-related environmental perturbations (e.g., rising temperatures) would facilitate terrestrial weathering as well, leading to a rapid increase of CIA values in Member I samples. Enhanced terrestrial weathering contributed large amounts of nutrients to the ocean (Mills et al., 2011; Wei et al., 2020) which would increase oceanic productivity (Wei et al., 2020) and lead to two significant consequences: (1) increasing organic matter burial on the seafloor and strong preservation of organic matter in sediments (Li et al., 2022), as supported by the high TOC levels in Member I samples, and (2) increasing dissolved O_2 levels in the surface ocean via photosynthesis ($CO_2 + H_2O \rightarrow CH_2O + O_2$). Organic matter shuttle would exhaust O_2 in the deep-water column, generating a large quantity of CO_3^{2-} ($CH_2O + O_2 \rightarrow CO_3^{2-} + 2H^+$) and producing anoxic conditions in the deep-water column (Wei et al., 2020). Sedimentary Mo has been widely used in

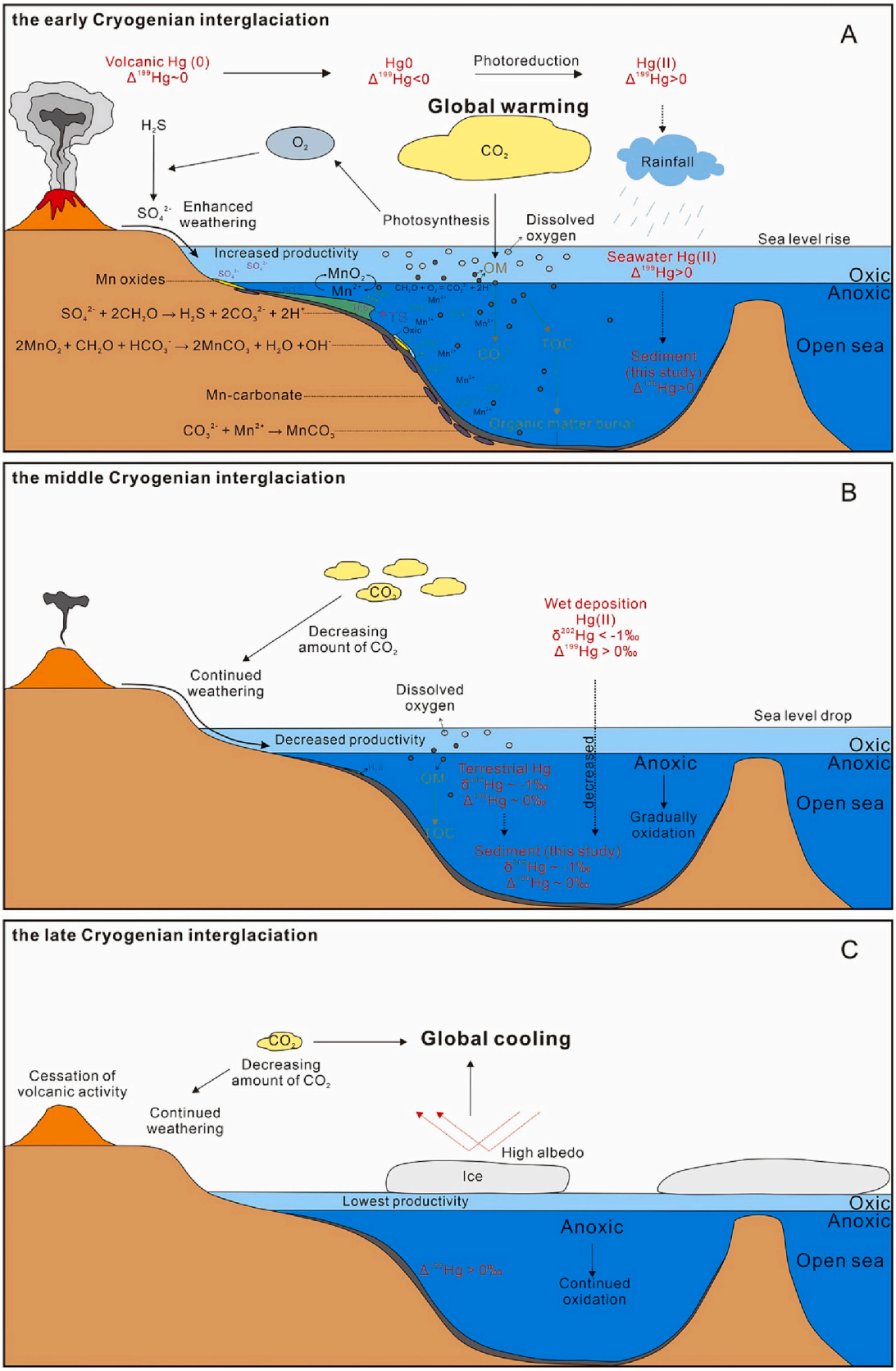

Fig. 4. Scenarios of environmental evolution during the Cryogenian interglaciation. (A) Large volcanism triggers greenhouse climate in the early Cryogenian interglaciation, leading to high dissolved oxygen levels in surface waters, high organic burial on the seafloor, and high terrestrial sulfate input into the ocean, which favors the deposition of rhodochrosite in Mn-bearing black shales; (B) Large-scale volcanism weakened in the middle-late Cryogenian interglaciation, leading to decreased dissolved oxygen levels in surface waters and decreased organic burial to the seafloor; (C) Continued continental weathering exhausted atmospheric CO_2 and drove the global climate to the Marinoan glaciation.

paleoceanographic studies as a redox proxy (Algeo and Lyon, 2006). The highest Mo concentrations (up to 42.5 ppm) and Mo/Al ratios (up to 5.23 ppm/wt%) in Member I samples suggest anoxic conditions in the deep-water column under the oxygenous surface ocean, which is consistent with the layered ocean model proposed by Li et al. (2012). The Mo/TOC characteristics of marine sediments were used to evaluate the Mo availability in deep water as well as the extent of basin restriction in many studies (Algeo and Lyons, 2006; Algeo and Rowe, 2012; Zhu et al., 2018; Cheng et al., 2018). Mo/TOC ratios reflect the degree of restriction in marine environments, with values of >35 ppm/%, 15–35 ppm/%, and < 15 ppm/% relating to weak, moderate, and strong restriction, respectively (Algeo and Lyons, 2006). The Mo/TOC ratios in Member I samples are <15 ppm/%, suggesting strong restriction of the Nanhua Basin (Fig. 5), consistent with the conclusion of Dangtangpo black shale in Minle samples (Cheng et al., 2018) and the paleogeographic reconstructions of Nanhua Basin (Wang and Li, 2003). In this semi-restricted anoxic basin, enhanced terrestrial weathering at this stage would contribute large amounts of sulfate (SO_4^{2-}) into seawater (Berner, 1982; Ma et al., 2019), which would also increase dissolved CO_3^{2-} levels in the water column and sulfide levels in sediments through the reduction of sulfate by organic matter in the water column ($SO_4^{2-} + 2CH_2O \rightarrow H_2S + 2CO_3^{2-} + 2H^+$) (Berner, 1982; Ma et al., 2019). The produced CO_3^{2-}, through the two above-mentioned pathways, would react with dissolved Mn^{2+} in the water column to form insoluble rhodochrosite ($CO_3^{2-} + Mn^{2+} \rightarrow MnCO_3$). In addition, increasing dissolved O_2 levels in the surface ocean via photosynthesis would cause the oxidation of Mn^{2+} to Mn oxides ($Mn^{2+} + 0.5O_2 + H_2O \rightarrow MnO_2 + H^+$), which were deposited to the seafloor and then reduced by organic matter to form Mn carbonates during early diagenesis ($2MnO_2 + CH_2O + HCO_3^- \rightarrow 2MnCO_3 + H_2O + OH^-$; Yu et al., 2016; Ma et al., 2019; Tan et al., 2021).

Stage II (Fig. 4B): The sharp decrease of Hg concentrations in Member II_1 samples would be explained by the decrease of their host phases (organic matter or sulfide) and may also suggest a weakening volcanism during the middle Cryogenian interglaciation. Consumed by terrestrial weathering, the atmospheric CO_2 levels decreased as well, leading to a dramatic decrease in oceanic productivity and organic matter burial on the seafloor, as supported by the decrease of TOC levels in the Member II_1 samples. A decline in organic matter burial would lead to decreased production of CO_3^{2-} and sulfides through the reduction of sulfate by organic matter in the water column, as supported by the low TS contents and the minor amounts of rhodochrosite in Member II samples. The characteristic of low Mo concentrations in Member II_1 samples is consistent with that observed in studies on the Datangpo samples (Li et al., 2012; Zhou et al., 2021; Pan et al., 2021). The Mo/TOC ratios in Member I samples are also lower than 15 ppm/%, suggesting strong restriction of the Nanhua Basin as well during this stage (Algeo and Lyons, 2006) (Fig. 5).

Stage III (Fig. 4C): Long-term consumption of atmospheric CO_2 by continental weathering, in the absence of large-scale volcanism, led to a decrease in atmospheric CO_2 and a cooling mode of the global climate that eventually drove the earth into the Marinoan glaciation. Global cooling and low atmospheric CO_2 levels during this stage caused the lowest oceanic productivity and the lowest organic matter burial on the seafloor, as supported by the lowest TOC levels in the Member II_2 samples. Sulfide contents at this stage would be the lowest as well, due to the lack of abundant organic matter to reduce seawater sulfate. The Mo/TOC ratios in Member II_2 samples may not provide sufficient constraints on the extent of basin restriction, due to the lack of correlation between Mo and TOC in Member II2 samples. However, we may infer an oxidative depositional environment in the Nanhua basin during this stage (Fig. 5), given that the lowest Mo concentrations of Member II2 samples are reflective of relative oxidizing water conditions (Algeo and Lyons, 2006).

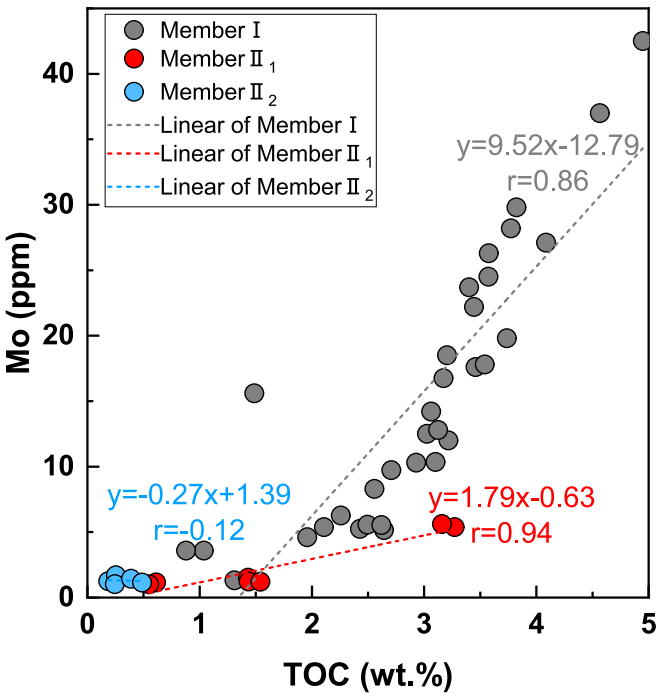

Fig. 5. Correlation between Mo and TOC in Cryogenian interglacial samples in drillcore ZK0202.

6. Conclusion

Through this study, several major points can be revealed: (1) Large volcanism triggers the termination of the Sturtian glaciation and the onset of Cryogenian interglaciation; (2) Greenhouse climate in the early Cryogenian interglaciation leading to high dissolved oxygen levels in surface waters, high organic burial on the seafloor and high terrestrial sulfate input into the ocean, which favors the deposition of rhodochrosite in Mn-bearing black shales; (3) Large-scale volcanism weakened in the middle-late Cryogenian interglaciation, leading to decreased dissolved oxygen levels in surface waters, decreased organic burial to the seafloor, which did not favor the deposition of rhodochrosite; (4) Continued continental weathering, in the absence of large-scale volcanism, exhausted atmospheric CO_2 and drove the global climate to the Marinoan glaciation. Overall, this study provides important insights into the climate-ocean-land dynamics during the Cryogenian interglaciation.

Declaration of Competing Interest

The authors declare that they have no known competing financial interestsor personal relationships that could have appeared to influence the work reported in this paper.

Data availability

Data will be made available on request.

Acknowledgments

This work was supported by the National key research and development program (2022YFC2903403).

Appendix A. Supplementary data

Supplementary data to this article can be found online at https://doi.org/10.1016/j.palaeo.2023.111634.

References

Algeo, T.J., Lyons, T.W., 2006. Mo-total organic carbon covariation in modern anoxic marine environments: Implications for analysis of paleoredox and paleohydrographic conditions. Paleoceanography 21, PA1016.

Algeo, T.J., Rowe, H., 2012. Paleoceanographic applications of trace-metal concentration data. Chem. Geol. 324–325, 6–18.

Bergquist, B.A., Blum, J.D., 2007. Mass-Dependent and Mass-Independent Fractionation of Hg Isotopes by Photoreduction in Aquatic Systems. Science 318, 417–420.

Berner, R.A., 1982. Burial of organic carbon and pyrite sulfur in the modern ocean; its geochemical and environmental significance. Am. J. Sci. 282, 451–473.

Blum, J.D., Bergquist, B.A., 2007. Reporting of variations in the natural isotopic composition of mercury. Anal. Bioanal. Chem. 388, 353–359.

Blum, J.D., Sherman, L.S., Johnson, M.W., 2014. Mercury Isotopes in Earth and Environmental Sciences. Annu. Rev. Earth Planet. Sci. 42, 249–269.

Cao, W., Lee, C.-T.A., Lackey, J.S., 2017. Episodic nature of continental arc activity since 750 Ma: a global compilation. Earth Planet. Sci. Lett. 461, 85–95.

Charbonnier, G., Adatte, T., Föllmi, K.B., Suan, G., 2020. Effect of intense weathering and postdepositional degradation of organic matter on Hg/TOC proxy in organic-rich sediments and its implications for deep-time investigations. Geochem. Geophys. Geosyst. 21, e2019GC008707.

Chen, D., Ren, D., Deng, C., Tian, Z., Yin, R., 2022. Mercury loss and isotope fractionation during high-pressure and high-temperature processing of sediments: Implication for the behaviors of mercury during metamorphism. Geochim. Cosmochim. Acta 334, 231–240.

Cheng, M., Li, C., Chen, X., Zhou, L., Algeo, T.J., Ling, H.F., Feng, L.J., Jin, C.S., 2018. Delayed Neoproterozoic oceanic oxygenation: evidence from Mo isotopes of the Cryogenian Datangpo Formation. Precambrian Res. 319, 187–197.

Ernst, R.E., Wingate, M.T.D., Buchan, K.L., Li, Z.X., 2008. Global record of 1600–700Ma large Igneous Provinces (LIPs): Implications for the reconstruction of the proposed Nuna (Columbia) and Rodinia supercontinents. Precambrian Res. 160, 159–178.

Fan, H., Fu, X., Ward, J.F., Yin, R., Wen, H., Feng, X., 2021. Mercury isotopes track the cause of carbon perturbations in the Ediacaran Ocean. Geology 49, 248–252.

Franzini, M., Leoni, L., Saitta, M., 1972. A simple method to evaluate the matrix effects in X-Ray fluorescence analysis. X-Ray Spectrom. 1, 151–154.

Grasby, S.E., Shen, W., Yin, R., Gleason, J.D., Blum, J.D., Lepak, R.F., Hurley, J.P., Beauchamp, B., 2017. Isotopic signatures of mercury contamination in latest Permian oceans. Geology 45, 55–58.

Grasby, S.E., Them, T.R., Chen, Z., Yin, R., Ardakani, O.H., 2019. Mercury as a proxy for volcanic emissions in the geologic record. Earth Sci. Rev. 196, 102880.

Hoffman, P.F., Abbot, D.S., Ashkenazy, Y., Benn, D.I., Brocks, J.J., Cohen, P.A., Cox, G. M., Creveling, J.R., Donnadieu, Y., Erwin, D.H., Fairchild, I.J., Ferreira, D., Goodman, J.C., Halverson, G.P., Jansen, M.F., Le Hir, G., Love, G.D., Macdonald, F. A., Maloof, A.C., Partin, C.A., Ramstein, G., Rose, B.E.J., Rose, C.V., Sadler, P.M., Tziperman, E., Voigt, A., Warren, S.G., 2017. Snowball Earth climate dynamics and Cryogenian geology-geobiology. Sci. Adv. 3, e1600983.

Hoffman, P.F., Kaufman, A.J., Halverson, G.P., Schrag, D.P., 1998. A Neoproterozoic snowball earth. Science 281, 1342–1346.

Krupp, R., 1988. Physicochemical aspects of mercury metallogenesis. Chem. Geol. 69, 345–356.

Li, C., Love, G.D., Lyons, T.W., Scott, C.T., Feng, L., Huang, J., Chang, H., Zhang, Q., Chu, X., 2012. Evidence for a redox stratified Cryogenian marine basin, Datangpo Formation, South China. Earth Planet. Sci. Lett. 331–332, 246–256.

Li, T., Zhu, G., Zhao, K., Chen, Z., 2022. Geochemical characteristics of organic-rich intervals within the Cryogenian non-glacial Datangpo Formation in southeastern Yangtze Block-implications for paleoenvironment and its control on organic matter accumulation. Precambrian Res. 378, 106777.

Li, Z.X., Bogdanova, S.V., Collins, A.S., Davidson, A., De Waele, B., Ernst, R.E., Fitzsimons, I.C.W., Fuck, R.A., Gladkochub, D.P., Jacobs, J., Karlstrom, K.E., Lu, S., Natapov, L.M., Pease, V., Pisarevsky, S.A., Thrane, K., Vernikovsky, V., 2008. Assembly, configuration, and break-up history of Rodinia: a synthesis. Precambrian Res. 160, 179–210.

Liu, Z., Tian, H., Yin, R., Chen, D., Gai, H., 2022. Mercury loss and isotope fractionation during thermal maturation of organic-rich mudrocks. Chem. Geol. 612, 121144.

Ma, Z., Liu, X., Yu, W., Du, Y., Du, Q., 2019. Redox conditions and manganese metallogenesis in the Cryogenian Nanhua Basin: Insight from the basal Datangpo Formation of South China. Palaeogeogr. Palaeoclimatol. Palaeoecol. 529, 39–52.

McKenzie, N.R., Horton, B.K., Loomis, S.E., Stockli, D.F., Planavsky, N.J., Lee, C.T., 2016. Continental arc volcanism as the principal driver of icehouse-greenhouse variability. Science 352, 444–447.

Mills, B., Watson, A.J., Goldblatt, C., Boyle, R., Lenton, T.M., 2011. Timing of Neoproterozoic glaciations linked to transport-limited global weathering. Nat. Geosci. 4, 861–864.

Moynier, F., Jackson, M.G., Zhang, K., Cai, H., Halldórsson, S.A., Pik, R., Day, J.M.D., Chen, J., 2021. The mercury isotopic composition of Earth's mantle and the use of mass independently fractionated Hg to test for recycled crust. Geophys. Res. Lett. 48, e2021GL094301.

Nesbitt, H.W., Young, G.M., 1982. Early Proterozoic climates and plate motions inferred from major element chemistry of lutites. Nature 299, 715–717.

Pan, W., Cao, M., Du, Y., Cheng, M., Zhou, Y., Algeo, T.J., Zhao, M., Thibault, N., Li, C., Wei, G., Dahl, T.W., 2021. Paired U and Mo isotope evidence for pervasive anoxia in the Cryogenian early interglacial ocean. Precambrian Res. 361, 106244.

Park, J., Stein, H.J., Georgiev, S.V., Hannah, J.L., 2022. Degradation of Hg signals on incipient weathering: Core versus outcrop geochemistry of Upper Permian shales, East Greenland and Mid-Norwegian Shelf. Chem. Geol. 608, 121030.

Qi, L., Hu, J., Gregoire, D.C., 2000. Determination of trace elements in granites by inductively coupled plasma mass spectrometry. Talanta 51, 507–513.

Rooney, A.D., Strauss, J.V., Brandon, A.D., Macdonald, F.A., 2015. A Cryogenian chronology: two long-lasting synchronous Neoproterozoic glaciations. Geology 43, 459–462.

Shen, J., Algeo, T.J., Chen, J., Planavsky, N.J., Feng, Q., Yu, J., Liu, J., 2019. Mercury in marine Ordovician/Silurian boundary sections of South China is sulfide-hosted and non-volcanic in origin. Earth Planet. Sci. Lett. 511, 130–140.

Shen, J., Chen, J., Algeo, T.J., Feng, Q., Yu, J., Xu, Y.-G., Xu, G., Lei, Y., Planavsky, N.J., Xie, S., 2020. Mercury fluxes record regional volcanism in the South China craton prior to the end-Permian mass extinction. Geology 49, 452–456.

Shen, J., Algeo, T.J., Feng, Q., 2022. Mercury isotope evidence for a non-volcanic origin of Hg spikes at the Ordovician-Silurian boundary, South China. Earth Planet. Sci. Lett. 594, 117705.

Tan, Z., Jia, W., Li, J., Yin, L., Wang, S., Wu, J., Song, J., Peng, P.A., 2021. Geochemistry and molybdenum isotopes of the basal Datangpo Formation: Implications for ocean-redox conditions and organic matter accumulation during the Cryogenian interglaciation. Palaeogeogr. Palaeoclimatol. Palaeoecol. 563, 110169.

Them II, T.R., Jagoe, C.H., Caruthers, A.H., Gill, B.C., Grasby, S.E., Gröcke, D.R., Yin, R. S., Owens, J.D., 2019. Terrestrial sources as the primary delivery mechanism of mercury to the oceans across the Toarcian Oceanic Anoxic Event (Early Jurassic). Earth Planet. Sci. Lett. 507, 62–72.

Wang, J., Li, Z., 2003. History of Neoproterozoic rift basins in South China: implications for Rodinia break-up. Precambrian Res. 122, 141–158.

Wei, G., Wei, W., Wang, D., Li, T., Yang, X., Shields, G.A., Zhang, F., Li, G., Chen, T., Yang, T., Ling, H., 2020. Enhanced chemical weathering triggered an expansion of euxinic seawater in the aftermath of the Sturtian glaciation. Earth Planet. Sci. Lett. 539, 116244.

Xu, L., Frank, A.B., Lehmann, B., Zhu, J., Mao, J., Ju, Y., Frei, R., 2019. Subtle Cr isotope signals track the variably anoxic Cryogenian interglacial period with voluminous manganese accumulation and decrease in biodiversity. Sci. Rep. 9, 15056.

Xue, W., Kwon, S.Y., Grasby, S.E., Sunderland, E.M., Pan, X., Sun, R., Zhou, T., Yan, H., Yin, R., 2019. Anthropogenic influences on mercury in chinese soil and sediment revealed by relationships with total organic carbon. Environ. Pollut. 255, 113186.

Xue, Z., Yin, R., Lehmann, B., Yang, R., Xu, H., Chen, J., Geng, H., Gao, J., 2022. Mercury isotopes reflect variable metal sources as a function of paleo-depositional setting in the Ediacaran-Cambrian Ocean, South China. Precambrian Res.,arch 378, 106749.

Yin, R., Feng, X., Meng, B., 2013. Stable Mercury Isotope Variation in Rice Plants (Oryza sativa L.) from the Wanshan Mercury Mining District, SW China. Environ. Sci. Technol. 47, 2238–2245.

Yin, R., Feng, X., Chen, B., Zhang, J., Wang, W., Li, X., 2015. Identifying the sources and Processes of Mercury in Subtropical Estuarine and Ocean Sediments using Hg Isotopic Composition. Environ. Sci. Technol. 49, 1347–1355.

Yin, R., Krabbenhoft, D.P., Bergquist, B.A., Wang, Z., Lepak, R.F., Hurley, J.P., 2016. Effects of Mercury and Thallium Concentrations on High Precision Determination of Mercury Isotope Composition by Neptune Plus Multiple Collector Inductively coupled Plasma Mass Spectrometry. J. Anal. At. Spectrom. 31, 2060–2068.

Yin, R., Xu, L., Lehmann, B., Lepak, R.F., Hurley, J.P., Mao, J., Feng, X., Hu, R., 2017. Anomalous mercury enrichment in early Cambrian black shales of South China: Mercury isotopes indicate a seawater source. Chem. Geol. 467, 159–167.

Yin, R., Chen, D., Pan, X., Deng, C., Chen, L., Song, X., Yu, S., Zhu, C., Wei, X., Xu, Y., Feng, X., Blum, J.D., Lehmann, B., 2022. Mantle Hg isotopic heterogeneity and evidence of oceanic Hg recycling into the mantle. Nat. Commun. 13, 1–7.

Yu, W., Algeo, T.J., Du, Y., Maynard, B., Guo, H., Zhou, Q., Peng, T., Wang, P., Yuan, L., 2016. Genesis of Cryogenian Datangpo manganese deposit: Hydrothermal influence and episodic post-glacial ventilation of Nanhua Basin, South China. Palaeogeogr. Palaeoclimatol. Palaeoecol. 459, 321–337.

Zambardi, T., Sonke, J.E., Toutain, J.P., Sortino, F., Shinohara, H., 2009. Mercury emissions and stable isotopic compositions at Vulcano Island (Italy). Earth Planet. Sci. Lett. 277, 236–243.

Zhang, Q., Chu, X., Bahlburg, H., Feng, L., Dobrzinski, N., Zhang, T., 2003. Stratigraphic architecture of the Neoproterozoic glacial rocks in the "Xiang-Qian-Gui" region of the Central Yangtze Block, South China. Prog. Nat. Sci. 13, 783–787.

Zhao, J., Li, Q., Liu, H., Wang, W., 2018. Neoproterozoic magmatism in the western and northern margins of the Yangtze Block (South China) controlled by slab subduction and subduction-transform-edge-propagator. Earth Sci. Rev. 187, 1–18.

Zhou, C., Huyskens, M.H., Lang, X., Xiao, S., Yin, Q., 2019. Calibrating the terminations of Cryogenian global glaciations. Geology 47, 251–254.

Zhou, T., Pan, X., Sun, R., Deng, C., Yin, R., 2021. Cryogenian interglacial greenhouse driven by enhanced volcanism: evidence from mercury records. Earth Planet. Sci. Lett. 564, 116902.

Zhu, G., Li, T., Zhao, K., Zhang, Z., Chen, W., Yan, H., Zhang, K., Chi, L., 2019. Excellent source rocks discovered in the Cryogenian interglacial deposits in South China: Geology, geochemistry, and hydrocarbon potential. Precambrian Res. 333, 105455.